Applied Catalysis B: Environmental 237 (2018) 957–969

Contents lists available at ScienceDirect

Applied Catalysis B: Environmental

journal homepage: www.elsevier.com/locate/apcatb

Promotion of catalytic selectivity on transition metal oxide through restructuring surface lattice

Juanjuan Liu[a,d,e,1], Victor Fung[b,1], Yong Wang[c], Kaimin Du[d], Shiran Zhang[a], Luan Nguyen[a], Yu Tang[a], Jie Fan[d,*], De-en Jiang[b,*], Franklin Feng Tao[a,*]

[a] Department of Chemical and Petroleum Engineering, University of Kansas, Lawrence, KS 66045, USA
[b] Department of Chemistry, University of California, Riverside, CA, USA
[c] School of Materials Science & Engineering, Zhejiang University, Hangzhou, PR China
[d] Department of Chemistry, Zhejiang University, Hangzhou, PR China
[e] College of Materials & Environmental Engineering, Hangzhou Dianzi University, Hangzhou 310036, PR China

ARTICLE INFO

Keywords:
Cobalt oxide
Selectivity
Surface faceting
Oxygen vacancies

ABSTRACT

Pursuit of high catalytic selectivity is paramount in the design of catalysts for green chemical processes towards minimizing the production of undesired products. We demonstrated that catalytic selectivity for production of alkene through oxidative dehydrogenation of alkane on transition metal oxides can be promoted through tailoring the surface lattice of the oxide catalyst. Selectivity for production of ethylene through oxidative dehydrogenation (ODH) of ethane on Co_3O_4 nanocrystals can be substantially increased by 30%–35% via temperature-mediated reconstruction of surface lattice of Co_3O_4. Co_3O_4 nanocrystals formed at 800 °C leads to smooth, flat crystal plane with predominantly exposed (111) facet in contrast to high Miller index (311) facet of Co_3O_4 formed at ≤700 °C, revealed by environmental transmission electron microscopy. Isotope-labelled experiments suggest that the higher catalytic selectivity on the (111) facet results from the lower activity of its surface lattice oxygen atoms. Consistent with these experimental results, DFT calculations suggest low activity of surface lattice oxygen atoms and high activation barriers for adsorption and dissociation of C—H bond on the (111) surface in contrast to (311). Upon the activation of C—H on (311), the stronger binding of ethylene on more active, under-coordinated surface lattice oxygen atoms of (311) forms a robust "deprotonated ethylene glycol"-like intermediate on (311) with a rate-limiting desorption barrier to the formation of ethylene. Compared to (311), the kinetically favorable desorption of bound ethylene species from (111) surface well rationalized the higher selectivity for production of ethylene on (111) than (311). These findings demonstrate that temperature-mediated tailoring of the surface lattice for a transition metal oxide nanocatalyst is a promising approach in pursuing high selectivity in oxidative dehydrogenation of hydrocarbons.

1. Introduction

Generally speaking, a fundamental understanding of catalysis on a heterogeneous catalyst largely relies on the identification of its surface structure at a molecular level or even at an atomic scale [1–6]. Mechanistic insights of elementary steps of a catalytic reaction performed on the surface of a heterogeneous catalyst including molecular adsorption, potential surface restructuring and product desorption, has been one of the main goals to pursue through experimental findings and theoretical simulations in the past decades. In terms of metal catalyst, it is generally acknowledged that the under-coordinated atoms of metal catalysts including atoms of step, edge, corner, kinks, or adatoms exhibit strong binding to adsorbates. In many cases these under-coordinated atoms are active sites [2,7–12]. Compared to extensive studies of a wide spectrum of metal catalysts in the last three decades [1,13], unfortunately much less attention was paid to the fundamental studies of catalytic mechanisms of oxide catalysts from surface science point of view.

Transition metal oxides, one of the most important class of heterogeneous catalysts, have been widely used in oxidative reactions [14–26]. One common feature of transition metal oxides is the existence of surface oxygen vacancies due to the existence of variable valence states [27–35]. Although more than half of industrial catalytic reactions are performed on transition metal oxides, fundamental

* Corresponding authors.
E-mail addresses: jfan@zju.edu.cn (J. Fan), djiang@ucr.edu (D.-e. Jiang), franklin.feng.tao@ku.edu (F.F. Tao).
[1] These authors made equal contribution to this work.

https://doi.org/10.1016/j.apcatb.2018.05.013
Received 22 October 2017; Received in revised form 12 April 2018; Accepted 5 May 2018
Available online 12 May 2018
0926-3373/

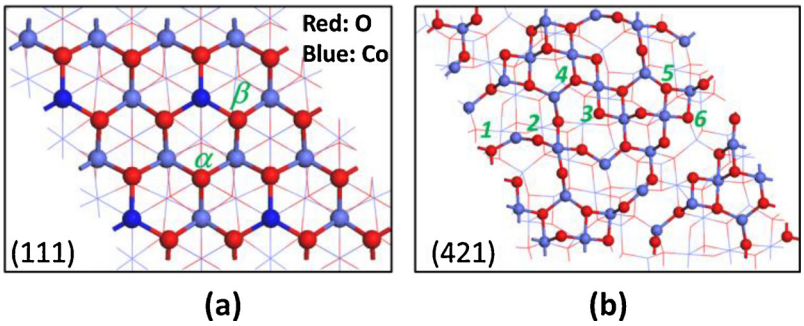

Fig. 1. Arrangement of oxygen atoms on optimized (111) and (421) surface of spinel-structure Co_3O_4. Two types of surface lattice oxygen atoms are shown with α and β in (a). Six types of surface lattice oxygen atoms are shown in 1, 2, 3, 4, 5, and 6 in.(b).

understanding of the surface structure at a molecular level and how the surface details of oxide catalysts at atomic scale are correlated to its catalytic selectivity are largely lacking. As expected, the distinct difference between the achieved depth of fundamental understanding of catalytic reactions on metal oxides and metals has resulted from the fact that complexity of transition metal oxide surfaces is higher than metal catalysts by two orders of magnitudes. First, surface of a transition metal oxide has both cations and anions. For instance, (111) and (421) surfaces exhibits quite different atomic packing of both oxygen anion and cobalt cations in Fig. 1. (421) has several types of surface lattice oxygen atoms (Fig. 1b). Secondly, most transition metal elements have multiple valence states and different valence states are coexistent in a crystallographic lattice in many cases. Thirdly, most transition metals can form oxides of different crystallographic phases; typically, these phases are transformable at different temperature or even at different catalytic conditions. For instance, spinel-structured Co_3O_4 is transformed to rock salt-structured CoO during catalysis in the mixture of NO and CO at 300 °C [36–40]. Additionally, bond strengths of M—O of many transition metal oxides are weaker than M—M bond of metal catalysts and thus M—O bonds could be cleaved readily under a relatively mild condition, which makes surface lattice oxygen atoms highly active. Thus, surface of transition metal oxide are typically oxygen atom or even metal atom-deficient. For oxidative catalysis, the chemical and coordination environments of surface lattice oxygen atoms are the key factors towards determining catalytic performance. Different from the complete oxidation of hydrocarbon producing the thermodynamically favorable final products CO_2 and H_2O, having an *appropriate* activity of surface lattice oxygen atoms of a catalyst is crucial for achieving high selectivity for ideal products of oxidative dehydrogenation (ODH) since partial oxidation is not the most thermodynamically favorable pathway. Thus, for ODH performed on a transition metal oxide, the activity of surface lattice oxygen atoms is the descriptor of the selectivity for producing ideal product of selective oxidation. From this point of view, tailoring chemical and coordination of surface lattice oxygen atoms is an important approach to tune selectivity of oxidative dehydrogenation.

Herein, we chose Co_3O_4 as a probe catalyst and ODH of ethane to produce ideal product of ethylene ($2C_2H_6 + O_2 = 2C_2H_4 + 2H_2O$) as a probe reaction. The by-product of this reaction is CO_2 formed in a complete oxidation of ethane. In this work, the correlation between catalyst surface structure and the catalytic performance of ODH of ethane to ethylene was systematically studied through both advanced in-situ/operando techniques and DFT simulation. We found that nanocrystals with either predominantly (111) or (311) surface facet formed through a treatment at a different temperature exhibit quite different selectivity for production of ethylene through ODH of ethane. The higher selectivity on (111) of Co_3O_4 than (311) by about 30%–35% was suggested to be intrinsically correlated with activity of surface lattice oxygen of the two types of surfaces. Isotopic exchange experiments of ^{18}O revealed that the capability to dissociate molecular oxygen at oxygen vacancies of Co_3O_4 (111) and to release surface lattice oxygen atoms from this surface is lower than high Miller index surface Co_3O_4 (311).

DFT calculations suggest that the distinct difference in catalytic selectivity between low Miller index surface (111) and high Miller index surface (311) intrinsically results from the quite different chemical and coordination environments of surface lattice oxygen at atomic scale on the two surfaces. The energy barrier for desorbing a monodeprotonated ethylene glycol-like stable intermediate to form product is higher than desorbing a similar immediate bound to (111) by 2.05 eV. The nearly barrier-less desorption of the intermediate, the CH_2-CH_2– on (111) makes (111) favorable for production of ethylene in contrast to (311). Both experimental and DFT studies demonstrated that surface faceting can be used as an approach to promote catalytic selectivity for ideal products of partial oxidation of hydrocarbons on transition metal oxides.

2. Experimental methods and DFT calculations

2.1. Synthesis of Co_3O_4 nanocrystal

Co_3O_4 nanocrystal was synthesized with a method reported in the literature [41,42]. 2.49 g of cobalt acetate tetrahydrate was dissolved into 30 mL of ethylene glycol and then the mixture was heated to 160 °C under vigorously stirring in N_2 atmosphere. Before the solution was refluxed for 1 h, 100 mL of 0.20 M $NaCO_3$ aqueous solution was added into the above mixture dropwise (1.11 mL min^{-1}). The purple products were obtained by centrifugation and washed by deionized water and ethanol for several times to make sure the Na was removed. After being dried at 50 °C overnight in a vacuum oven, pure Co_3O_4 nanocrystals were obtained by calcinations at certain temperature (*T*) in air for 4 h, which was label as Co_3O_4-*T*.

2.2. Characterizations

Powder X-ray diffraction (XRD) patterns were recorded on a Rigaku Ultimate IV operating in reflection mode with Cu *Kα* radiation with XRF mode. The nitrogen sorption measurements were performed on an ASAP 2010 unit (Micromeritics) at 77 K after activation at 150 °C for 3 h. TEM and HRTEM images were recorded on the TECNAI G2 F20 operated at 200 kV. In situ environmental TEM was performed inside an environmental transition electron microscope (h-9500, Hitachi). This microscope was equipped with a bottom mounted direct detection camera (DE-12, direct electron) and a time resolution of 10 frames per second was used for the in situ recording. Temperature-programmed reduction (TPR) tests were carried out in a Micromeritics Autochem 2910 equipped with a TCD detector.

The oxygen isotope-exchange experiments were conducted using the same fixed-bed flow reactor on-line coupled to a quadrupole mass spectrometer for on-line analysis of the gas composition at the

downstream of the fixed-bed flow reactor. The quadrupole mass spectrometer can readily distinguish $^{16}O_2$ (m/z = 32), $^{18}O_2$ (m/z = 36) and $^{16}O^{18}O$ (m/z = 34). Before preparation of isotope-labelled catalysts, the Co_3O_4 catalyst precursor was calcined at 350, 600, 700, or 800 °C in air. Then, these Co_3O_4 catalysts were annealed in $^{18}O_2$ at a temperature same as its calcination temperature in air (350, 600, 700 or 800 °C) for 0.5 h, by which the isotopic labelled catalysts were prepared. The as-prepared isotope-labelled catalysts were purged with N_2 for 1 h to eliminate the $^{18}O_2$, $^{16}O^{18}O$ and $^{16}O_2$ until the mass spectrometer signals of $^{18}O_2$, $^{16}O^{18}O$, $^{16}O_2$ returned to the base line. Then, 5.0% $^{16}O_2$ was introduced to flow through the catalyst; the temperature was raised from 30 to 600 °C at a heating rate of 20 °C min^{-1} to perform a potential oxygen exchange between ^{16}O and ^{18}O. When one peak appeared at a temperature T_0, the sample was further annealed with a ramping rate of 20 °C min^{-1} until there was no further increase in the intensity of $^{16}O^{18}O$ at a temperature T_m; then, the sample was being kept at T_m until there was no more $^{16}O^{18}O$ formed; in other words, the signal of $^{16}O^{18}O$ went back to the original baseline. Then, the catalyst was annealed to a higher temperature with a ramping rate of 20 °C min^{-1} until the next peak appeared.

2.3. Measurements of catalytic performances

All measurements of catalytic performances of oxidative dehydrogenation of ethane to ethylene on pure Co_3O_4 catalysts were performed in a fixed bed reactor operating at atmosphere pressure. They were conducted in the temperature range of 350–600 °C with 0.05 g of catalyst diluted with 0.50 g of quartz sand. The quartz sand was purified by aqua regia solution and then washed with deionized water for several times. The inner diameter of the test tube is 6.0 mm. The sources of the reactant gases are 10.0% C_2H_6/Ar and 10.0% O_2/Ar. 25.0 mL min^{-1} of 10.0% C_2H_6 and 25.0 mL min^{-1} 10.0% O_2 were mixed and then introduced to the fixed-bed flow reactor. Gas composition of the mixture of reactant gases entering this fixed-bed flow reactor is 5/5/90 for C_2H_6/O_2/Ar. Ethane and reaction products were analyzed on-line with a gas chromatograph equipped with a FID detector. Blank experiments were performed on 0.55 g quartz sand in the same fixed-bed flow reactor while the mixture of reactants was introduced. Conversions of < 1.0% at 350 °C and of < 2.0% at 600 °C were found for the 0.55 g quartz sand. Experimental errors of the measurements of conversion and selectivity are ± 5% of the reported conversion and selectivity, respectively. Carbon balances were in the range 100% ± 5%.

To interpret the suppression of the activity of surface lattice oxygen atoms of Co_3O_4 by high calcinations temperature, complete oxidation of ethane to CO/H_2O and/or CO_2/H_2O was conducted between 200 °C and 600 °C on 0.050 g catalyst diluted with 0.50 g purified quartz sand. The reactant gases were 10 mL min^{-1} of 10.0% C_2H_6/Ar and 40 mL min^{-1} of 10.0% O_2/Ar. The feedstock composition was 2/8/90 for C_2H_6/O_2/Ar. Ethane and ethylene were analyzed with an on-line gas chromatograph equipped with a FID detector.

2.4. DFT calculations

All DFT calculations were performed using the Vienna ab initio Simulation Package (VASP) [43,44]. The Perdew-Burke-Erzerhof (PBE) [45] functional of generalized-gradient approximation (GGA) was used for electron exchange and correlation. The electron-core interaction was described using the projector-augmented wave method (PAW) [46,47]. We used the DFT + U method reported by Dudarev et al. [48] in VASP using a Hubbard parameter of U = 2 eV for Co, because their calculations yielded a band gap and local spin moments on Co^{2+} and Co^{3+} sites in close agreement with the experiment, as shown in a previous work [41,42]. A kinetic energy cutoff of 450 eV was used for the planewaves, and the Brillouin zone was sampled using a 3 × 3 × 1 Monkhorst-Pack scheme [49]. All calculations in this work were performed with spin polarization. Bulk Co_3O_4 is antiferromagnetic at low temperature and transitions to a paramagnetic state above 40 K. To model the paramagnetic state of Co_3O_4, we used the ferromagnetic (FM) spin state as approximation.

Adsorption energies were calculated by using the definition $E_{ads} = E_{surface+adsorbate} - (E_{surface} + E_{adsorbate})$, where the energy of the adsorbate $E_{adsorbate}$ was computed by placing the adsorbate in a 10 Å wide vacuum cubic cell which is sufficiently wide enough to prevent intermolecular interactions from the periodic boundary conditions. Transition states were found via first optimizing the approximate reaction coordinate using the nudged elastic band method (NEB) and then using the dimer method [50] for a force convergence of 0.05 eV/Å. In the high-temperature range of this study (700–800 °C), we assume the harmonic approximation to the transition-state theory. In this case, the temperature dependence expressed in the term exp(-E_a/kT), while the prefactor is temperature-independent, is determined by the ratio of normal-mode frequency products at the initial and transition states. For similar reactions on the two surfaces in question, the prefactors determined by the frequencies are usually similar; thus, we can assume the main factor in dictating selectivity would be the difference in E_a.

3. Results and discussion

3.1. Surface morphology of fresh and used Co_3O_4 nanocrystals

Co_3O_4 nanocrystals were prepared by a modified wet chemistry method with a followed annealing in O_2. Fig. 2 presents the XRD patterns of fresh and used Co_3O_4 catalysts prepared by calcination at different temperatures in purified air. Here, "*fresh Co_3O_4*" designates a catalyst experienced a calcination in air at certain temperature for 4 h but this catalyst has not been used for catalysis. A "*used Co_3O_4*" refers to a fresh catalyst which ***has previously undergone*** catalysis (ODH) in the temperature range of 400–600 °C in a fixed-bed flow reacor. The temperatures after the terms of "used Co_3O_4", "used catalyst", "fresh Co_3O_4" or "fresh catalyst" in the text are the *calcination temperature of the catalyst* in air before catalysis. Notably, this calcination temperature in terms *used Co_3O_4-T* such as *used Co_3O_4-800 °C* is different from catalysis temperature which is always in the range of 400–600 °C in this work.

All these diffraction patterns of fresh and used Co_3O_4 shown in Fig. 2 can be well indexed to the standard diffraction patterns of Co_3O_4 (PDF 43–1003) [51–53]. The average crystallite sizes of the fresh and used Co_3O_4 crystals were calculated by Scherrer equation. As listed in

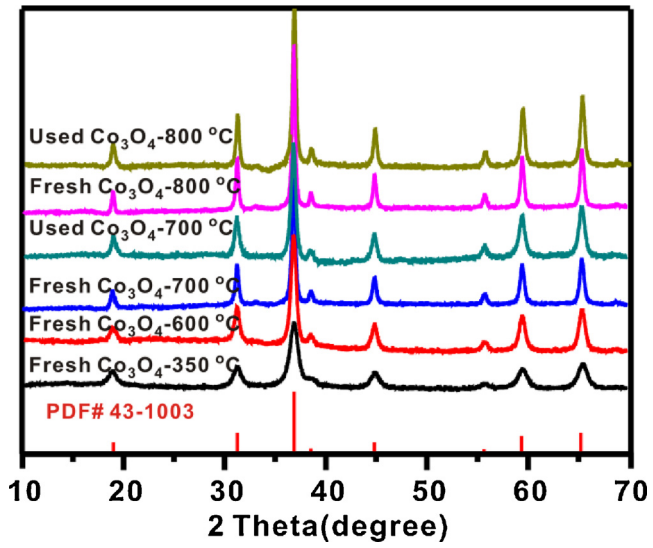

Fig. 2. XRD patterns of fresh Co_3O_4-T and used Co_3O_4-T (T = 350 - 800 °C) catalysts.

Table 1
Surface areas and average crystallite sizes of fresh Co_3O_4 and used Co_3O_4 catalysts.

Entry	Sample	Average Crystallite Size (nm)[b]	Surface Area (m^2 g^{-1})
1	Fresh-Co_3O_4-350 °C	12.9	118
2	Used-Co_3O_4-350 °C	—	56[a]
3	Fresh-Co_3O_4-600 °C	14.2	63
4	Used-Co_3O_4-600 °C	—	54
5	Fresh-Co_3O_4-700 °C	18.9	41
6	Used-Co_3O_4-700 °C	18.0	39
7	Fresh-Co_3O_4-800 °C	21.0	37
8	Used-Co_3O_4-800 °C	19.7	33

[a] The sharp decrease in surface area of used Co_3O_4-350 °C is due to the high catalysis temperature (600 °C).
[b] The average sizes of crystallites are calculated by the Scherrer equation from XRD data in Fig. 2.

Table 1, the sizes of used Co_3O_4-*T* gradually increase with the calcination temperature (*T*), likely due to the sintering.

Besides, as shown in Table 1, a high calcination temperature decreases specific surface area of the series of fresh-Co_3O_4 and that of used-Co_3O_4 largely. The decreasing surface area with the increase of annealing temperature may result from the particle sintering at high temperature. The N_2 adsorption-desorption isotherms in Fig. S1 show that all of the fresh/used Co_3O_4 samples are of type IV with an H1 hysteresis loop, which are observed for mesoporous materials with packing holes. Notably, our catalyst does not have intrinsic mesopores although Co_3O_4 with intrinsic mesopores was reported in literature [54]. The surface area of the used-Co_3O_4-350 °C is largely lower than the fresh-Co_3O_4-350 °C since the high catalysis temperature range up to 600 °C is higher than the calcination temperature, 350 °C. In terms of the catalysts calcined at higher temperatures (600, 700, or 800 °C), there is little difference in surface areas between fresh-Co_3O_4-*T* and used-Co_3O_4-*T*. In other words, because the catalyst nanocrystals have been sintered in the step of calcinations at 600, 700, or 800 °C, the subsequent catalysis at 400–600 °C couldn't sinter the Co_3O_4 nanocrystals any further. In addition, catalysts calcined at 700 °C (entries 5 and 6 of Table 1) and catalysts calcined at 800 °C (entries 7 and 8) exhibt similar surface area in the range of 32.5–41.1 m^2 g^{-1}. It suggests there was no further sintering from 700 to 800 °C.

Although there is very little change in the macroscopic property in terms of surface area (m^2 g^{-1}) between the series of fresh-Co_3O_4-700 °C and used-Co_3O_4-700 °C and the series of fresh-Co_3O_4-800 °C and used-Co_3O_4-800 °C, the surface morphologies of these nanocrystals calcined at 700 °C and 800 °C are quite different. The Co_3O_4 nanocrystal calcined at 800 °C has a remarkably flatter and more even surface. To explore the impact of calcination temperatures on the surface morphologies of Co_3O_4 nanocrystals, in situ environmental TEM studies were carried out to track the evolution of surface morphologies and crystallographic facets along the increase of catalyst temperature in O_2/N_2 mixture with a presssure ratio of 1:4 at 10 mbar. It is noted that the micrographs in Fig. 3 were captured from the in situ TEM movie and unfortunately some of them were out of focus as nanoparticles were not stable in such high temperature conditions. The structural evolution of the particles was very fast at high temperatures. To catch the fast structural evolution, we couldn't have time to adjust the focus.

Fig. 3a–c present representative structural evoltuions of different Co_3O_4 nanocrystals from 700 °C to 800 °C, respectively. Clearly, as the temperature of Co_3O_4 nanocrystals was increased from 700 °C (Fig. 3a1–c1) to 800 °C (Fig. 3a3, b3 and c2), the original rough surface develops substantially sharper and better-defined edges and corners. The obvious change of surface structure of Co_3O_4 nanocrystals in this temperature range suggests that the surface atoms were evolved from the higher index rough surface at 700 °C to lower index smooth surface at 800 °C. Unfortunately, collection of atom-resolved TEM images with

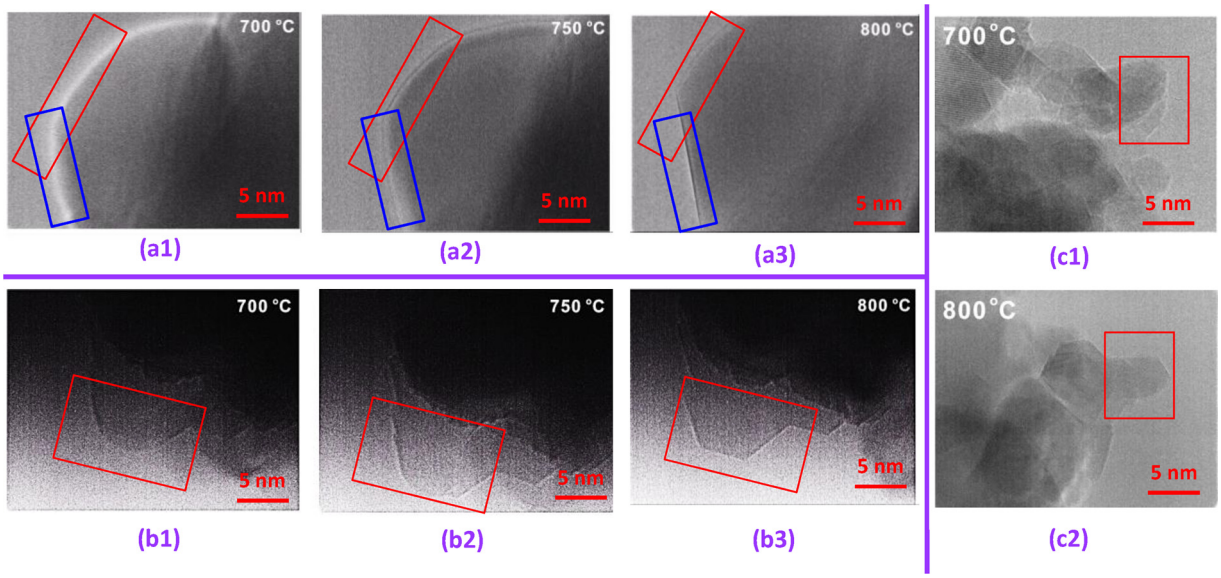

Fig. 3. Evolution of surface morphology of the same Co_3O_4 nanocrystals during calcination in the mixture of O_2 and N_2 (O_2/N_2 gas) along the increase of calcination temperature. Nanocrystals of Co_3O_4 in images of each series (a, b or c) is the same. The feature of these evolutions of surface morphology of these nanocrystals is the much better flatness and smoothness of the surface of Co_3O_4 along the increase of calcination temperature from 700 to 800 °C. The highly flattened faceting of Co_3O_4 nanocrystals can be readily identified in TEM images (a3), (b3) and (c2). All images of this figure were collected at the indicated temperature in the mixture of O_2 and N_2 on an environmental TEM system.

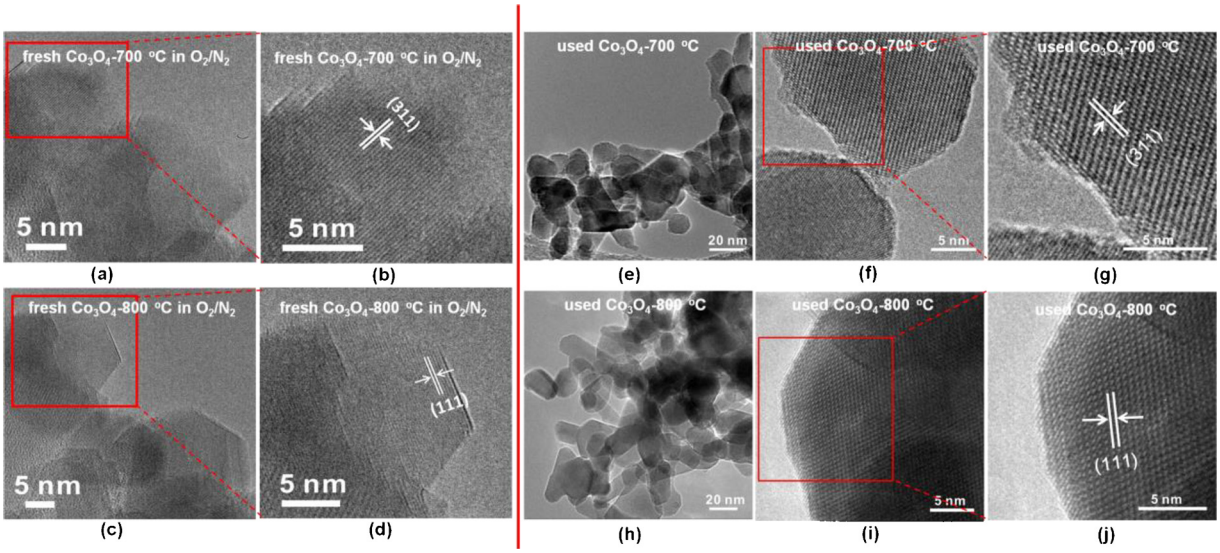

Fig. 4. ETEM and TEM studies of Co_3O_4 nanocrystals. (a and b) TEM images with 1D lattice fringe of fresh-Co_3O_4-700 °C in O_2/N_2. (c and d) TEM images with 1D lattice fringe of fresh- Co_3O_4-800 °C in O_2/N_2. (e) TEM image of large scale sample area of the used- Co_3O_4-700 °C. (f and g) High-resolution TEM image of the used-Co_3O_4-800 °C with 2D lattice fringe. (h) TEM image of large-scale sample area of the used-Co_3O_4-800 °C. (i and j) High-resolution TEM image of the used-Co_3O_4-800 °C with 2D lattice fringe.

two-dimensional lattice fringe of Co_3O_4 nanocrystals during annealing at 700 and 800 °C in the O_2/N_2 atmosphere is significantly challenging. However, our TEM images of one dimernsional fringes were sucessfully collected during calcination at 700 and 800 °C in the O_2/N_2 atmosphere. Compared to the nanocrystals at 700 °C in O_2/N_2 (Fig. 4a and b), sufaces of these nanocrystals at 800 °C in O_2/N_2 are largely smoothed as shown in Fig. 4c and d. These in-situ ETEM studies clearly suggest the formation of a smooth surface with (111) faceting (Fig. 4d). This is because the high thermal energy provided to the surface of nanocrystals at a higher temperature makes surface atoms readily across the diffusion barrier to form a more thermodynamically favorable surface. As it has been extremely challenging in achieving high resolution TEM images with *two-dimensional* lattice fringes during catalysis conditions at 600 °C in the mixture of ethane and O_2, we identifed the lattice fringes of the used-Co_3O_4-700 °C and the used-Co_3O_4-800 °C at room temperature in UHV. A close examination of these two-dimensional fringes found that the surface morphologies of the nanocrystals of the used-Co_3O_4-700 °C (Fig. 4e – g) always exhibit rougher and less well-defined edges than the nanocrystals of the used-Co_3O_4-800 °C (Fig. 4h–j), suggesting that used-Co_3O_4-700 °C has a noticeably rougher surface with more defect sites than the used-Co_3O_4-800 °C.

As shown in Fig. 4g, the lattice fringes of the used-Co_3O_4-700 °C display inter-planar spacing of 0.243 nm, which match well with those of the (311) crystal facets of Co_3O_4.[55] Compared to the feature of the used-Co_3O_4-700 °C (Fig. 4e–g), the surface morphologies of the used-Co_3O_4-800 °C are quite different as shown in Fig. 4h–i. The surface of the used-Co_3O_4-800 °C is markedly smoother (Fig. 4f of 700 °C versus Fig. 4i of 800 °C and Fig. 4g of 700 °C versus Fig.4j of 800 °C). Fig. 4j is one representative image of the high-resolution images collected from the same pot of the catalyst (used-Co_3O_4-800 °C). Based on the representative lattice fringe images of Co_3O_4 nanocrystals (used-Co_3O_4-800 °C), the preferentially exposed surface of used-Co_3O_4-800 °C is (111). Thus, the predominant facets of used-Co_3O_4-700 °C and used-Co_3O_4-800 °C should be (311) and (111), respectively. In addition, we also extensively studied the morphology of the used-Co_3O_4-600 °C and the used-Co_3O_4-350 °C. For the used-Co_3O_4-700 °C, used-Co_3O_4-600 °C and used-Co_3O_4-350 °C, the mainly exposed facetings are high Miller index surface. Different from them, the mainly exposed surface of the used-Co_3O_4-800 °C is (111) (Fig. 4i and j). As shown in the next section, high Miller index surface of used-Co_3O_4-T (T = 600 or 700 °C) and lower Miller index surface of Used-Co_3O_4-800 °C exhibit quite different catalytic selectivities for oxidative dehydrogenation of ethane to ethylene.

3.2. Catalytic perfomances of Co_3O_4 nanocrysals

Selective oxidative dehydrogenation (ODH) of ethane to ethylene was employed as a probe reaction to explore the intrinsic correlation between surface structure and catalytic performance of Co_3O_4-T (T = 600–800 °C) catalysts. Fig. S2 plots the C_2H_6 conversion versus weight hourly space velocity (WHSV). The linear relationship between conversion of ethane and WHSV validated that the catalytic reaction was conducted in the kinetic regime. As shown in Fig. 5a, the conversions of ethane on Co_3O_4-600 °C and Co_3O_4-700 °C catalysts are similar in the temperature range of catalysis (400–600 °C), likely due to the approximately similar surface structure of Co_3O_4-600 °C and Co_3O_4-700 °C (entries 4 and 6 in Table 1). Interestingly, the conversions of ethane on Co_3O_4-800 °C catalyst at a catalysis temperature < 500 °C are in stark contrast to those on Co_3O_4-700 °C, although surface area of the Co_3O_4-800 °C is lower than Co_3O_4-700 °C by 10% or so. For instance, the converison of C_2H_6 on Co_3O_4-800 °C at the catalysis temperature of 400 °C, 6.6%, is only one quarter of the ethane conversion on Co_3O_4-700 °C at the same catalysis temperature, 24.1%. At the catalysis temperature of 450 °C, the conversion on Co_3O_4-800 °C, 13.1%, is only half of Co_3O_4-700 °C, 25.6%.

Based on the propsoed mechanism in literature [56,57], the C_2H_5 intermediates formed on the surface could desorb to gas phase and then dissociate into C_2H_4 through collision with reactant molecules in gas phase (homogeneous catalysis) or with inert species of the catalyst surface at a high temperature (heterogeneous catalysis). Along the increase of catalysis temperature, homogeneous catalysis-like mechnaism is dominant at a higher temperature. Mathematically the surface area of the used Co_3O_4-800 °C (32.5 m^2/g) is 17% lower than used Co_3O_4-700 °C (39.1 m^2/g). At a catalysis temperature lower than 500 °C, heterogeneous catalysis plays a dominant role; the surface structure of (111) of Co_3O_4-800 °C exhibits a low conversion due to its low surface area. At a catalysis temperature higher than 500 °C, the larger role of homogeneous catalysis-like mechansis on Co_3O_4-800 °C than Co_3O_4-700 °C makes the conversion on Co_3O_4-800 °C higher than Co_3O_4-700 °C.

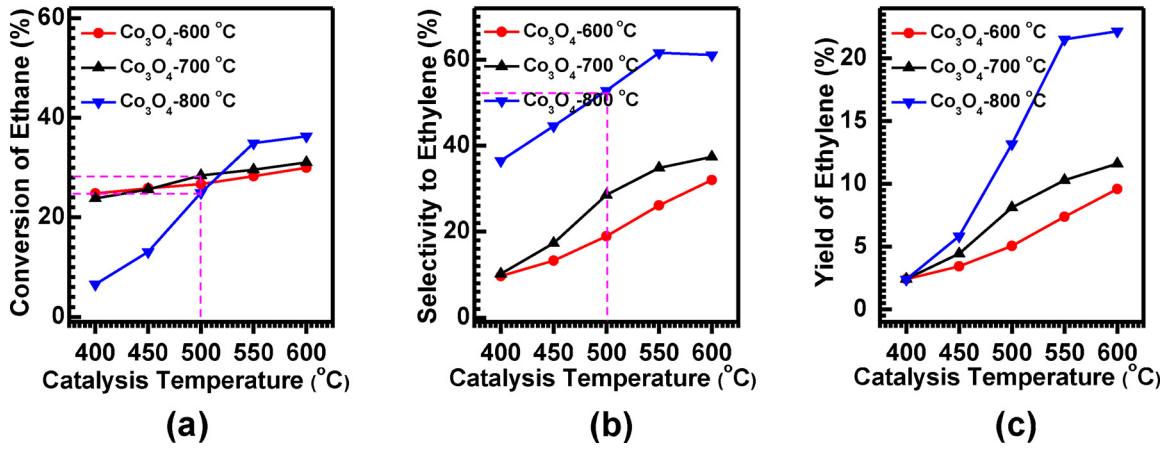

Fig. 5. Catalytic performance of Co_3O_4-*T* (*T*: calcination temperature, *T* = 600–800 °C) in the temperature range of 400–600 °C. (a) Conversion of ethane; (b) Catalytic selectivity for production of ethylene; (c) yield of ethylene on Co_3O_4-*T* catalysts. In each study, 0.050 g catalysts diluted with 0.50 g quartz sand was loaded to the same fixed-bed flow reactor; the C_2H_6 (10% balanced with Ar) with a flow rate of 25.0 mL min^{-1} and O_2 (10% balanced with Ar) with a flow rate of 25.0 mL min^{-1} were mixed and then introdcued to the upstream of the fixed-bed flow reactor.

Besides the difference in conversion of ethane in 400–500 °C, the distinct difference between the two catalysts is the selectivity for production of ethylene, the ideal product of ODH of ethane. As shown in Fig. 5b, the selectivities of ethylene on Co_3O_4-800 °C catalyst in the catalysis temperature range of 400 – 600 °C are much higher than those on other catalysts such as Co_3O_4-700 °C and Co_3O_4-600 °C. Even if the conversions of ethane on all three Co_3O_4 catalysts (Co_3O_4-600 °C, Co_3O_4-700 °C and Co_3O_4-800 °C) are almost identical (25–28%) at the catalysis temperature of 500 °C (Fig. 5a), their selectivities are distinctly different (Fig. 5b). The selectivity of ethylene on Co_3O_4-800 °C at the catalysis temperature of 500 °C is nearly 25% higher than that of Co_3O_4-700 °C (53.0% versus 28.5%). These comparisons clearly suggest the low Miller index surface formed at 800 °C contributed to the high catalytic selectivity for the production of ethylene.

It is interesting to note that the selectivity increases along with the increase of catalysis tempature for all samples. According to literatures [56,57], there are two possible reaction mechanisms for oxidative dehydrogenation of ethane. One is the pure heterogeneous catalysis mechanism. In specific, ethane molecules can be activated on certain sites of the surface of a catalyst, forming C_2H_5 radicals, which subsequently react with the very active species (O^-, O_2^- or O^{2-}) in the surface lattice to form OC_2H_5 interemdiates. The as-formed OC_2H_5 intermediate could cleave a C—O bond to form a C_2H_4 molecule on the catalyst surface, followed by the desorption of C_2H_4 to the gas phase as an ideal product. Meanwhile, OC_2H_5 intermediates formed on the surface could be further oxidized by active oxidizing species of the surface to form CO or CO_2, which decreases catalyctic selectvity for production of ethylene. Generally, at a relatively low temperature, the pure heterogenous catalysis mechanism is predominant.

The other mechanism is the so-called heterogeneous-homogeneous mechanism. The C_2H_5 intermediates formed on the surface could desorb to gas phase and then dissociate into C_2H_4 through collision between radical and reactant molecules in a gas phase or between radical and inert species of the catalyst surface at a high temperature. Along the increase of catalyst temperature, the residence time of C_2H_5 on a catalyst surface will largely decrease and thus readily desorb to gas phase. Thus, at a higher temperature the contribution of heterogeneous-homogeneous catalysis to the production of ethylene is larger. As a result, the overall catalytic selectvity for formation of ethylene through ODH increases along the increase of a catalysis temperature, accompanied by the increase of ethane conversion (Fig. S4).

Fig. 5c plots the yield of ethylene as a funcion of catalysis temperature on Co_3O_4-600 °C, Co_3O_4-700 °C, and Co_3O_4-800 °C. The yields of ethylene on Co_3O_4-800 °C (blueline) are noticeably higher than other Co_3O_4 catalysts in the catalysis temperature range of 400–600 °C. Interestingly, while the surface areas of the used-Co_3O_4-700 °C and the used-Co_3O_4-800 °C are similar (39.1 m^2g^{-1} *vs.* 32.5 m^2g^{-1}), Co_3O_4-800 °C catalyst produces twice amount of ethylene of Co_3O_4-700 °C catalyst (11.6% versus 22.2% at catalysis temperature 600 °C). This difference must result from their different facetings in terms of different exposed surfaces, (111) of Co_3O_4-800 °C versus (311) of Co_3O_4-700 °C. From surface science point of view, each catalytic event is performed on specific surface sites of a catalyst. The topmost surface of (111) of Co_3O_4-800 °C and (311) of Co_3O_4-700 °C have both suface lattice oxygen anion and cobalt cations. Thus, the distinctly different catalytic selectivities must result from the different activity of surface lattice oxgen atoms and oxygen vacancies. Isotope-labelled exchange of surface lattice oxygen atoms on surfaces of the used-Co_3O_4-700 °C and used-Co_3O_4-800 °C will provide a measure of the activities of the two surfaces. O/Co ratios of surfaces of two catalysts during catalysis were measued with AP-XPS. As discussed in Section 3.3, a correlation between surface structure of the two catalysts and their corresponding catalytic selectivities was esablished.

3.3. *Difference in activity of surface lattice oxygen atoms of the two facets of Co_3O_4 nanocrystals*

H_2-TPR tests were performed to investigate the difference in properties of being reduced. Catalysts Co_3O_4-600 °C, Co_3O_4-700 °C and Co_3O_4-800 °C show two main reduction peaks around 292 °C (the sharp one, peak a in Fig. S5) and 384 °C (the broader one, peak b in Fig. S5), which are attributed to the reduction of Co_3O_4 to CoO and of CoO to Co, respectively. In comparison to Co_3O_4-800 °C, the reduction behaviors of Co_3O_4-600 °C and Co_3O_4-700 °C are different. The two redcution peaks shifted to higher temperature along with the increase of calcinations temperature of Co_3O_4-*T*. It suggests that the capabilities reducing catalyst Co_3O_4 to CoO and CoO to Co are suppressed along the incrrease of annealing temperature. This trend is actually consistent with the better surface crystallization in terms of formation of low Miller index surface at a higher temperature such as 800 °C.

The oxygen isotopic-exchange experiments were carried out on isotopic labelled $Co_3{}^{16}O_{4-x}{}^{18}O_x$-350 °C, $Co_3{}^{16}O_{4-x}{}^{18}O_x$-600 °C, $Co_3{}^{16}O_{4-x}{}^{18}O_x$-700 °C and $Co_3{}^{16}O_{4-x}{}^{18}O_x$-800 °C ($0 < x < 1$) to explore any potential difference in activity of surface lattice oxygen atoms of these catalysts. Along with the increase of annealing temperature of an isotope-labelled catalyst, surface lattice oxygen atoms can hop and couple to each other to form molecuar oxygen and then desorb. When $^{16}O^{16}O$ gas flows through a ^{18}O labelled catalyst in a fixed-flow reactor,

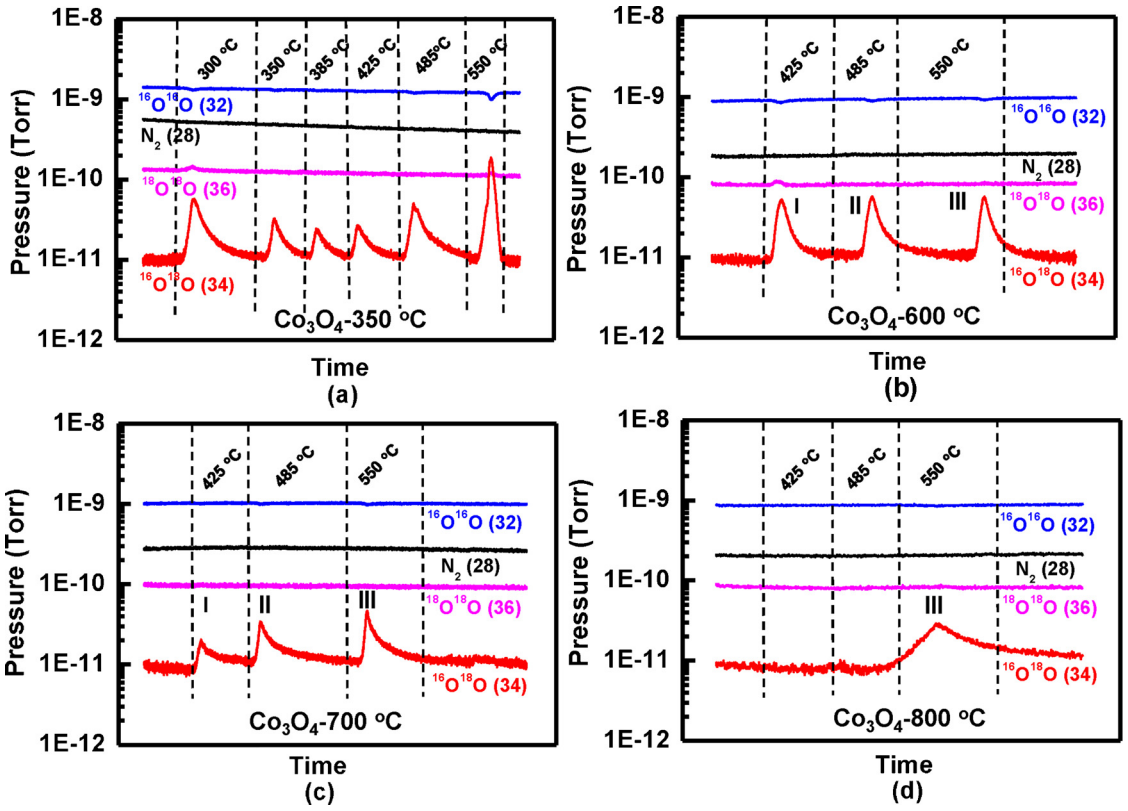

Fig. 6. Mass spectra of $^{16}O^{18}O$ on $Co_3{}^{16}O_{4-x}{}^{18}O_x$-T (T = 350, 600, 700 and 800 °C) catalysts in the temperature range of 30–600 °C recorded during the exchange of surface oxygen atoms of catalysts with flowing $^{16}O_2$. (a) $Co_3{}^{16}O_{4-x}{}^{18}O_x$-350 °C; (b) $Co_3{}^{16}O_{4-x}{}^{18}O_x$-600 °C; (c) $Co_3{}^{16}O_{4-x}{}^{18}O_x$-700 °C; (d) $Co_3{}^{16}O_{4-x}{}^{18}O_x$-800 °C.

molecular oxygen$^{16}O^{16}O$ in the flowing gas could dissociate on surface oxygen vacancies of the isotope-labelled catalyst and thus the dissoicated oxygen atoms could be captured by the catalyst through filling oxygen vacancies as surface lattice oxygen atoms; then, the captured ^{16}O atoms on the surface could hop and couple with other surface oxygen atoms including the native ^{16}O and ^{18}O atoms of the isotope-labelled catalyst to form $^{16}O^{16}O$ and $^{16}O^{18}O$ molecules, respectively, and then desorb at a some temperature to gas phase. These desorbed oxygen molecules can be collected and analyzed by the mass spectrometer connected to the downstream of the fixed flow reactor. Notably, variation of intensity of $^{16}O^{16}O$ at these temperatures of desorbing $^{16}O^{18}O$ could not clearly identified due to the logarithm scale of Y-axis of the partial pressure. As only small portion of oxygen atoms of Co_3O_4 were replaced by ^{18}O atoms during preparation of $Co_3{}^{16}O_{4-x}{}^{18}O_x$, the amount of $^{18}O^{18}O$ formed through exchange of $^{16}O^{16}O$ with ^{18}O of $Co_3{}^{16}O_{4-x}{}^{18}O_x$ is definitely smaller than $^{16}O^{18}O$. Thus, the desorption of $^{18}O^{18}O$ was not clearly observed.

Surface lattice oxygen atoms of different surfaces would have quite different hoping barriers; oxygen vacancies of different surfaces would have different activity and thus the activation barrier for dissociating moelcular oxygen on different surface vacanceies could be different. The activities of surface lattice oxygen atoms and oxygen vacancies deterimine the desorption temperature of oxygen molecules from this surface. By finding the desorption temperature of oxygen molecules leaving the surface, the activity of surface lattice oxygen atoms of the surface can be deduced. By comparing the desorption temperatures of (311) and (111), the difference in activty of surface lattice oxygen atoms of these catalysts can be uncovered.

Experimentally, the temperauure for forming isotope-labelled oxygen molecules $^{16}O^{18}O$ or $^{18}O^{18}O$ can be found out by monitoring the evolution of partial pressure of the $^{16}O^{18}O$ or $^{18}O^{18}O$ molecules along the increase of the temperature of isotope-labelled Co_3O_4 in $^{16}O_2$. Undoubtedly, a lower desorption temperature of $^{16}O^{18}O$ or $^{18}O^{18}O$ suggests that the desorbed molecular oxygen was formed from a type of more active surface lattice oxygen (in terms of a weaker binding to Co cations) which can desorb via a lower barrier, or from a surface oxygen vacancy which can readily dissociate molecular O_2 at a lower temperature.

As shown in Fig. 6a, six peaks of $^{16}O^{18}O$ were observed (300, 350, 385, 425, 485, and 550 °C) during isotope exchange studies on the $Co_3{}^{16}O_{4-x}{}^{18}O_x$-350 °C, suggesting the high roughness of $Co_3{}^{16}O_{4-x}{}^{18}O_x$-350 °C due to the relatively low calcination temperature, 350 °C. Meanwhile, only three desorption peaks of $^{16}O^{18}O$ at 425, 485, and 550 °C were observed on Co_3O_4-600 °C and Co_3O_4-700 °C catalysts in Fig. 6b and c. The desorptions of $^{16}O^{18}O$ formed through exchange of surface lattice oxygen atoms at 425, 485, and 550 °C are denoted as I, II and III, respectively in Fug. 6b and 6c. Surprisingly, only desorption peak III was observed on Co_3O_4-800 °C catalyst as shown in Fig. 6d. This difference suggests that the capability of the Co_3O_4 surface in dissociating molecular oxygendepends largely on the calcination temperature of this catalyst used in its preparation. In other words, Co_3O_4-800 °C has a low capability in releasing surface lattice oxygen atoms in terms of breaking Co–O bonds. These isotope exchange studies show that the possibility of breaking the Co–O bond in terms of activity of surface lattice oxygen atoms can be greatly decreased by calcinating the Co_3O_4 nanocrystals at 800 °C, a temperature approaching the melting point of Co_3O_4.

The lack of desorption peak of $^{16}O^{18}O$ from Co_3O_4-800 °C at < 550 °C suggests that the low activity of surface lattice oxygen atoms of Co_3O_4-800 °C in contrast to these Co_3O_4 calcined at 700 °C or at a lower temperature. The lower activity of surface lattice oxygen atoms of Co_3O_4-800 °C than Co_3O_4-700 °C (or Co_3O_4-700 °C, Co_3O_4-600 °C) was further confirmed by the lower catalytic activity of Co_3O_4-800 °C than Co_3O_4-700 °C in complete oxidation of ethane to CO_2 and H_2O. Deep oxidation of ethane was performed on Co_3O_4-800 °C than Co_3O_4-700 °C. As can be seen in Fig. 7, the T_{50} value, defined as the

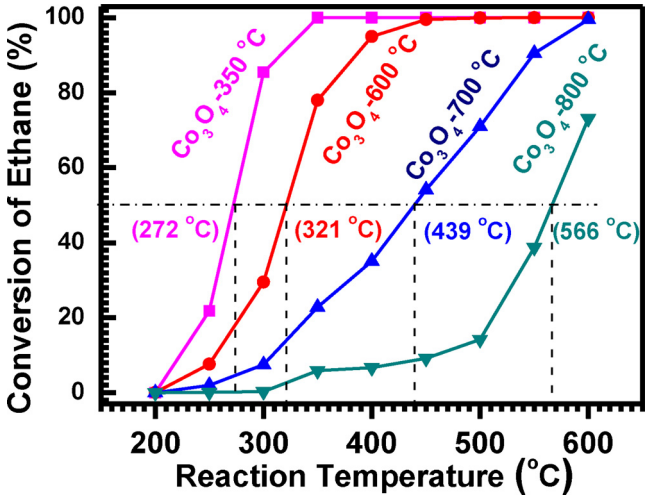

Fig. 7. Catalytic performance of deep oxidation of ethane on Co_3O_4-T (T = 350, 600, 700, and 800 °C) catalysts (The catalyst weight is 0.05 g diluted with 0.50 g quartz sand; the flow rate of C_2H_6 (10%) is 10.0 mL min^{-1} and the flow rate of O_2 (10%) is 40.0 mL min^{-1}).

temperature where the conversion reaches 50%, increases rapidly from 321 °C of Co_3O_4-600 °C, 439 °C of Co_3O_4-700 °C to 566 °C of Co_3O_4-800 °C, suggesting that Co_3O_4 calcined at a higher temperature exhibits a lower catalytic activity in deep oxidation of ethane. Notably, although the surface areas of Co_3O_4-700 °C and Co_3O_4-800 °C are similar (entries 5–8 in Table 1), T_{50} of Co_3O_4-700 °C is lower than that of Co_3O_4-800 °C by 127 °C. Consistently, the conversion of ethane on Co_3O_4-800 °C at catalysis temperature of 500 °C is only 14.2% while it is 71% on Co_3O_4-700 °C at the same catalysis temperature. Undeniably, Co_3O_4-700 °C catalyst is much more active than Co_3O_4-800 °C for the complete oxidation of ethane. It shows the catalytic activity of surface lattice oxygen atoms of Co_3O_4-700 °C is definitely higher than Co_3O_4-800 °C. In other words, the surface lattice oxygen atoms of (311) are more active than (111) in the complete oxidation of C_2H_6. This high activity of surface oxygen of (311) in complete oxidation rationalizes the observed high conversion of ethane during ODH on Co_3O_4-700 °C than Co_{34}-800 °C but low selectivity for production of ethylene on Co_3O_4-700 °C (Fig. 5a and b).

The better crystallization of surface region of Co_3O_4 nanocrystals was uncovered by in-situ environmental TEM and high resolution TEM (Fig. 3 and 4). In fact, the well crystallization of Co_3O_4-800 °C is also supported by surface sensitive analytic techniques with the capability of examining a catalyst surface, ambient pressure X-ray photoelectron spectroscopy (AP-XPS).

In-situ studies of Co_3O_4 nanocrystals under reaction condition in pure O_2 using AP-XPS confirmed that the density of oxygen vacancies on surface of Co_3O_4-*T* is lower if the calcination temperature (*T*) is higher. By assuming the O/Co ratio of Co_3O_4-800 °C in O_2 is 1.33, the O/Co atomic ratios on surfaces of Co_3O_4-*T* were calculated and plotted as a function of surface temperature (Fig. 8c). As shown in Fig. 8c, the O/Co ratio of surface region of Co_3O_4 nanocrystals calcined at a lower temperature is lower. Along the increase of calcination temperarue in O_2/N_2, the O/Co ratio is increased. It clearly suggests that surface of Co_3O_4 calcined at a higher temperature such as 800 °C has a lower density of oxygen vacancies. This is consistent with formation of a less-defective surface of Co_3O_4-800 °C as suggested by environmental TEM studies.

Fig. 8 presents the photoemission features of Co 2*p*, O1*s* and the atomic ratio of O to Co. In terms of Co 2*p*, there is no obvious shift of the main peak at 777.5 eV as seen by reference to the vertical red line in Fig.8a. O 1*s* photoemission feature includes a main peak at 530.2 eV and a shoulder at high binding energy side. It could be assigned to surface hydroxyl group as the referee indicated. On the other hand, the nonstoichiometric oxygen of Co_3O_4 could be another source of the shoulder since the O/Co ratios of Co_3O_4-350 °C, Co_3O_4-450 °C, and Co_3O_4-700 °C are lower than 1.33. Thus, we tend to consider that the shoulders of Co_3O_4-350 °C or Co_3O_4-450 °C were contributed from both the nonstoichiometric oxygen atoms and OH group. In terms of Co_3O_4-800 °C, likely majority of OH groups could have been desorbed. Thus, OH groups do not obviously contribute to the shoulder of O 1*s* of Co_3O_4-800 °C. The difference in the feature of O 1 s shoulder between Co_3O_4-800 °C and Co_3O_4-700 °C likely results from the change of surface structure in terms of chemical and coordination environment of surface lattice oxygen atoms. As both the oxygen atoms of OH group and the oxygen atoms of near to oxygen vacancy (called nonstoichiometric oxygen) contributed to the shoulder of the O 1*s* of Co_3O_4 and the contribution of OH groups is variable at different temperature, it is challenging to deconvolute the O 1*s* spectra of Co_3O_4 and comparison of the composition of O 1*s* shoulders of the two types of catalysts may not provide valuable information. Here, the O 1*s* photoemission features of Fig. 8b were not deconvoluted.

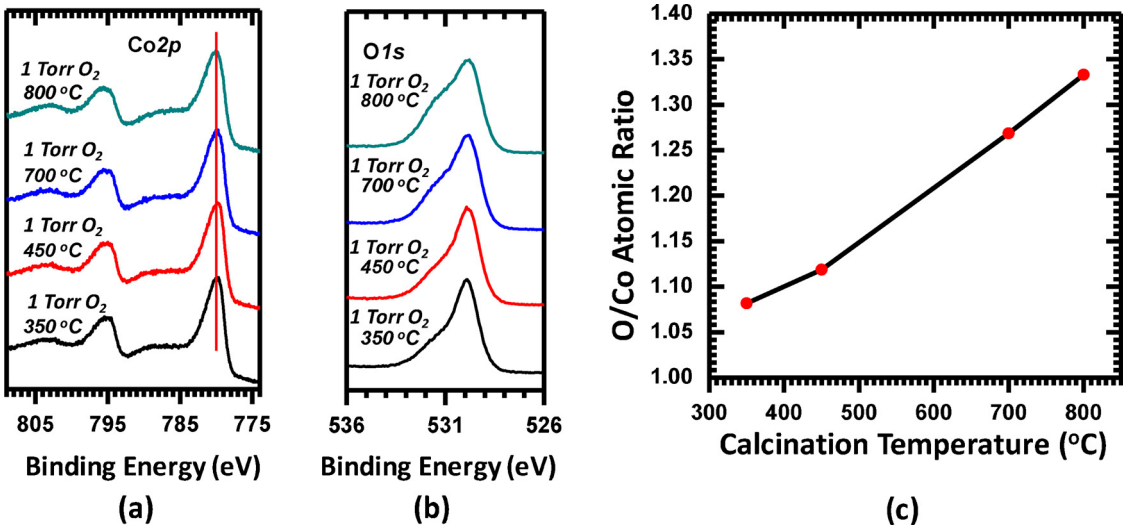

Fig. 8. In-situ studies of Co_3O_4 nanocrystals annealing at different temperatures (from 350 to 800 °C) in O_2. (a) Co 2p. (b) O 1 s. (c) Atomic ratio of O/Co of surface of Co_3O_4 calcined at different temperature; these ratios were calculated by assuming that O/Co ratio of Co_3O_4 calcined at 800 °C in O_2 is stoichiometric, 1.33.

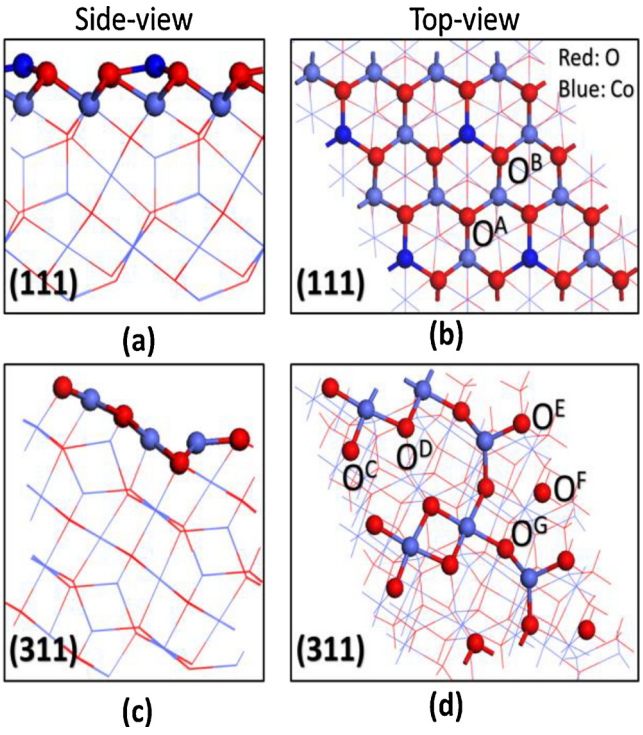

Fig. 9. Surface structure of (111) and (311) facets of Co_3O_4. The inequivalent surface lattice oxygen atoms are label in the top view.

3.4. DFT calculations

We have identified the difference in surface structure of the two types of catalysts through structural characterizations at the nano/atomic scale through in situ environmental TEM and confirmed the resultant difference in activity of activating molecular oxygen by using ensemble techniques at macroscopic scale including isotope exchange studies and in-situ surface studies with AP-XPS. For the purpose of understanding the difference between catalytic selectivity for production of ethylene from ethane on (311) and (111) at a molecular level, here we used DFT calculations to probe the reaction pathways and then establish an intrinsic correlation between surface structure, catalytic selectivity, and reaction pathway. In the following DFT calculations, the experimentally observed (111) surface was used to represent the low Miller index surface of the catalyst, Co_3O_4-800 °C, and the (311) surface for high Miller index surface of catalyst, Co_3O_4-700 °C. Bare (111) and (311) surfaces have several possible surface terminations. We determined which termination is the most stable under the ODH condition (see Table S1 in Supporting Information for details) with *ab* initio thermodynamics to calculate the surface energies [58]. The most stable terminations to represent (111) and (311) from our calculated surface energies (Table S1) are shown in Fig. 9. From the calculated surface energies, the (111) termination is significantly lower in energy than the (311) surface, and is consistent with the observation of surface reconstruction from (311) to (111) through high temperature annealing.

As shown in Fig. 9, one can identify two types of inequivalent surface lattice oxygen atoms on the most stable (111) surface (marked as O^A and O^B) and five types of inequivalent lattice oxygen atoms on the (311) surface (marked as O^C, O^D, O^E, O^F and O^G). Formation energies of different oxygen vacancies on (111) and (311) were calculated. As shown in Table 2, formation energies of oxygen vacancies on (311) are lower than (111), suggesting that the bond strengths of Co–O on (311) are weaker than on (111) and thereby the surface lattice oxygen atoms on (311) are more active than on (111). This supports our experimental finding that the (311) facet of $Co_3{}^{16}O_{4-x}{}^{18}O_x$-700 °C can dissociate $^{16}O^{16}O$ at 425 °C and 485 °C but the (111) facet of $Co_3{}^{16}O_{4-x}{}^{18}O_x$-800 °C cannot. In addition, DFT calculations show that surface lattice oxygen atoms of (311) exhibits higher adsorption energy to H atoms and CH_3 than (111) as shown in Table 2.

To fundamentally understand the difference in catalytic selectivity for production of ethylene through oxidative dehydrogenation on (311) and (111), three reaction routes were proposed as shown in Fig. 10a. Both the A→B→E and the A→C→F routes are a full oxidation to CO_2, whereas the A→C→D pathway forms the ideal product, ethylene.

We first studied step A in Fig. 10a, the cleavage of the first C—H of C_2H_6, on the most active oxygen sites: O^A of (111) and O^C of (311) (Fig. 9). Both the heterolytic mechanism over a Co^{2+}–O or Co^{3+}–O pair and homolytic mechanism via a single lattice O atom were considered. Five binding configurations of dissociated C_2H_5 and H on (111) and seven on (311) were explored; the calculated activation barriers and reaction energies for activating the first C—H of ethane on (111) and (311) were listed in entries 1–5 in Table S2 for (111) and entries 6 – 12 for (311). On (311), the lowest barrier is 0.40 eV (entry 10 in Table S2), while on (111) the lowest barrier is 0.62 eV (entry 3 in Table S2). On (111), the reaction occurs over the O^A site, homolytically cleaving the C—H bond and resulting in an ethyl radical that is then reabsorbed to a nearby oxygen (see structures ii and iii in Fig. 11a). On (311), the reaction occurs over a similar mechanism in its corresponding O^C on the surface (see structures ii and iii of (311) in Fig. 11c). These results are also consistent with our descriptor predictions shown in Table 2, which showed O^A of (111) and O^C of (311) as the most reactive oxygen for C—H activation. From the difference in activation energies of the first C—H bond, it is evident that the complete oxidation of ethane will occur at a higher temperature over the (111) facet than the (311) facet, which agrees well with the higher experimental ethane T_{50} temperatures on the Co_3O_4-800 °C (Fig. 7).

For routes A→B→E and the A→C→F, we searched transition states for activating the first C—H (step A) and the second C—H (step B or C) on both (311) and (111). Energy profiles of theses located transition states and optimized final states of step A were presented in Fig. 11b. Following the Step A, the ODH reaction of ethane can then proceed via the subsequent C—H cleavage from either its α carbon (step B) or its β

Table 2
Descriptors of oxygen activity for the non-identical oxygen of the (111) and (311) facets.[a].

Entry	Surface of Co_3O_4	Oxygen atom	Number of Co atoms around the O atom	Vacancy formation energy (eV)	H adsorption energy (eV)	CH_3 adsorption energy (eV)
1	111	**A**	**3**	**2.49**	**—3.61**	**—2.57**
2	111	B	3	3.02	—3.46	—2.12
3	311	**C**	**2**	**0.76**	**—4.28**	**—3.21**
4	311	D	3	2.14	—3.50	—2.38
5	311	E	3	2.15	—3.87	—2.83
6	311	F	3	2.53	—3.69	—2.45

[a] Oxygen E on the (311) surface is not listed as it is 4 coordinated and partially obscured by nearby atoms. The bolded entry denotes the oxygen with the highest predicted activity for each facet.

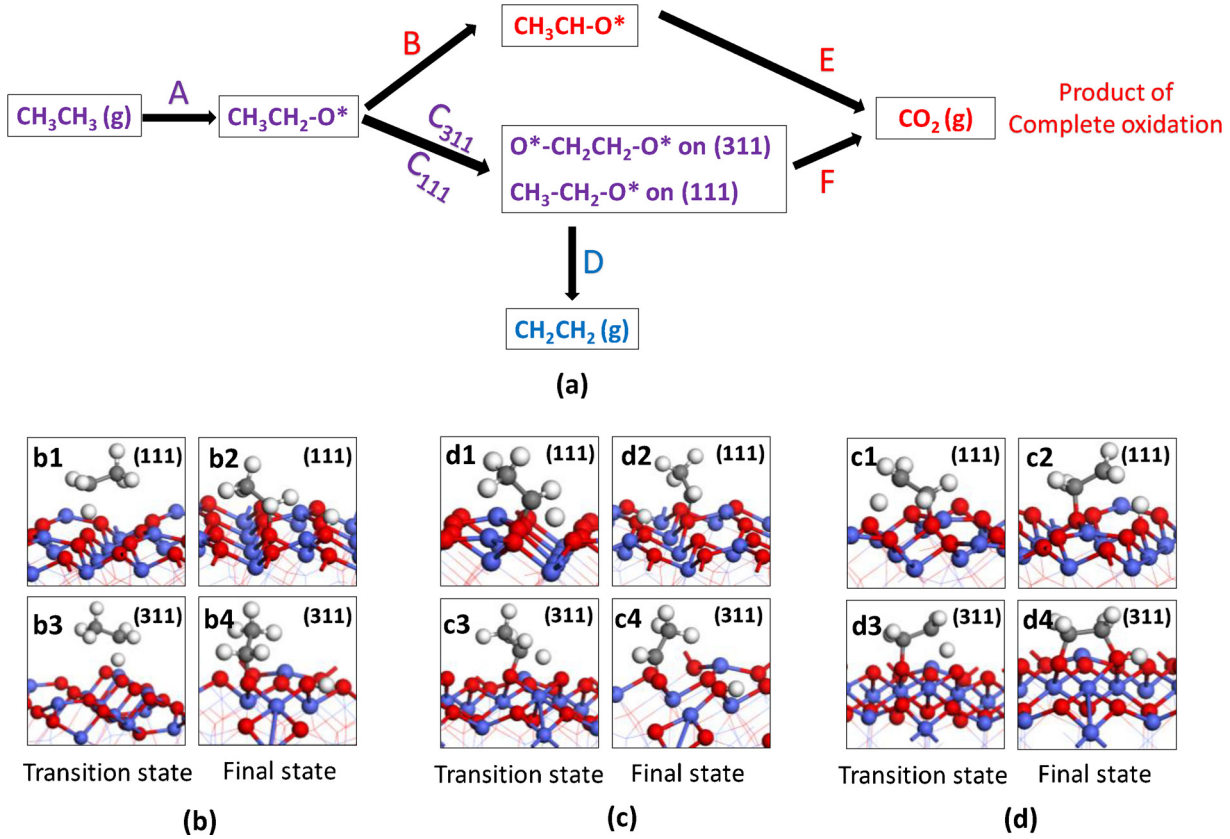

Fig. 10. Potential reaction routes and schematic of intermediates and transition state of steps A, B and C towards a full oxidation product, CO_2 or production of ethylene through ODH on (111) and (311). (a) Schematics of reaction routes (A-B-E and A-C-F) leading to a complete oxidation of ethane to form CO_2 and (A-C_{311}-D or A-C_{111}-D)) leading to ideal product ethylene through ODH of ethane; each box gives the intermediate. (b) Transition state and final state of step A, the activation of the first C–H to form adsorbed CH_3CH_2–O* and H–O*–. (c) Transition state and final state of step B, the activation of the second C–H to form adsorbed CH_3CH–O* and H–O*–. (d) Transition state and final state of step C, the activation of the second C–H to form adsorbed CH_3CH_2–O* and H–O*– on (111) (d1 and d2) or to form adsorbed O*–CH_2CH_2–O* and H–O*– on (311) (d3 and d4).

carbon (step C) (Fig. 10a). The activation barriers of step B are 0.87 and 0.30 eV for the (111) and (311) surfaces, respectively, while those of step C are 1.20 and 0.55 eV for (111) and (311), respectively (Table 2). Thermodynamically, the formation of the intermediate, CH_3CHO– (step B) or –O–CH_2CH_2–O– (step C) on (311) is energetically favorable. The reaction energies for forming the CH_2CH_2O– or –O–CH_2CH_2–O– intermediates on (311) are −1.77 eV and −1.52 eV, respectively; however, they are higher in energy at −0.37 eV and 1.01 eV on (111), respectively. Fig. 11c presents the energy profile of oxidative dehydrogenation through A→C→D. Undoubtedly, the energy of the intermediate –O–CH_2CH_2–O– formed on (311) through step C is much lower than that of CH_2–CH_2–O– on (111) (v in Fig. 11c). Structural parameters of the optimized intermediate v formed on (111) and (311) are listed in Fig. 11c.

Step B results in the formation of an adsorbed acetaldehyde, CH_3CH–O– which will likely not result in formation of ethylene, whereas step C results in an adsorbed –O–CH_2–CH_2–O– which may desorb through breaking –O–C bonds to form ethylene. Thus, we further explored the step D in Fig. 10a through DFT calculations. The calculations of energy profile and activation barriers for pathway A→C→D on both (111) and (311) are listed in Fig. 11d and Table 3. One can see that after step C (the formation of –O–CH_2–CH_2–O– on (311) and CH_2–CH_2–O– on (111)), C_2H_4 spontaneously desorbs from (111) to form the gas-phase product in step D through breaking the C–O*– bond with a ΔH of −0.82 eV. Here O* denotes surface lattice oxygen atoms. In contrast, –CH_2–CH_2– is strongly adsorbed on (311) through the structure v in Fig. 11d. It bonds with two oxygen atoms of the surface (311). The activation barrier to desorb the bound –CH_2–CH_2– from (311) to form ethylene is as high as 2.18 eV with a ΔH of 1.96 eV. This is likely due to the high activity of surface lattice oxygen atoms. Compared to the essentially barrierless step of desorbing ethylene on (111) to gas phase (red dashed line in Fig. 11d), the quite high barrier for desorbing bound ethylene on (311) (blue dashed line in Fig. 11d) results in a low selectivity for producing ethylene on (311). The different adsorption capability of (111) and (311) is well consistent with the kinetic studies (Fig. S6). A much lower ethylene reaction order was obtained on Co_3O_4-800 °C as compared to Co_3O_4-700 °C, indicating a weaker adsorption of ethylene on Co_3O_4-800 °C than on Co_3O_4-700 °C.

The much stronger ethylene adsorption on the (311) surface (structure v in Fig. 11b and c) allows for an easier subsequent oxidation of –CH_2–CH_2– to CO_2. Obviously, the (311) surface does not take the route of desorbing ethylene, A→C→D. In contrast, the very weak adsorption of ethylene on the (111) surface suggests a much higher likelihood of directly desorbing ethylene from (111) surface of Co_3O_4 to gas phase before it can be further oxidized. We therefore conclude that both the strong bonding of –CH_2–CH_2– on (311) in the format of a "monodeprotonated ethylene glycol"-like species (Fig. S8a) and the higher activation energy to desorb –CH_2–CH_2– to form CH_2-CH_2 are the key reasons for its low selectivity for production of ethylene. Besides, based on the propsoed mechanism in literature, [56,57] homogeneous catalysis-like mechnaism is dominant at a higher temperature. The strong bonding of –CH_2–CH_2– on (311) and the higher activation energy to desorb –CH_2–CH_2– might therefore lead to low activity at high temperature (> 500 °C), as extensively discussed in section 3.2.

By understanding the difference between (111) and (311) at atomic

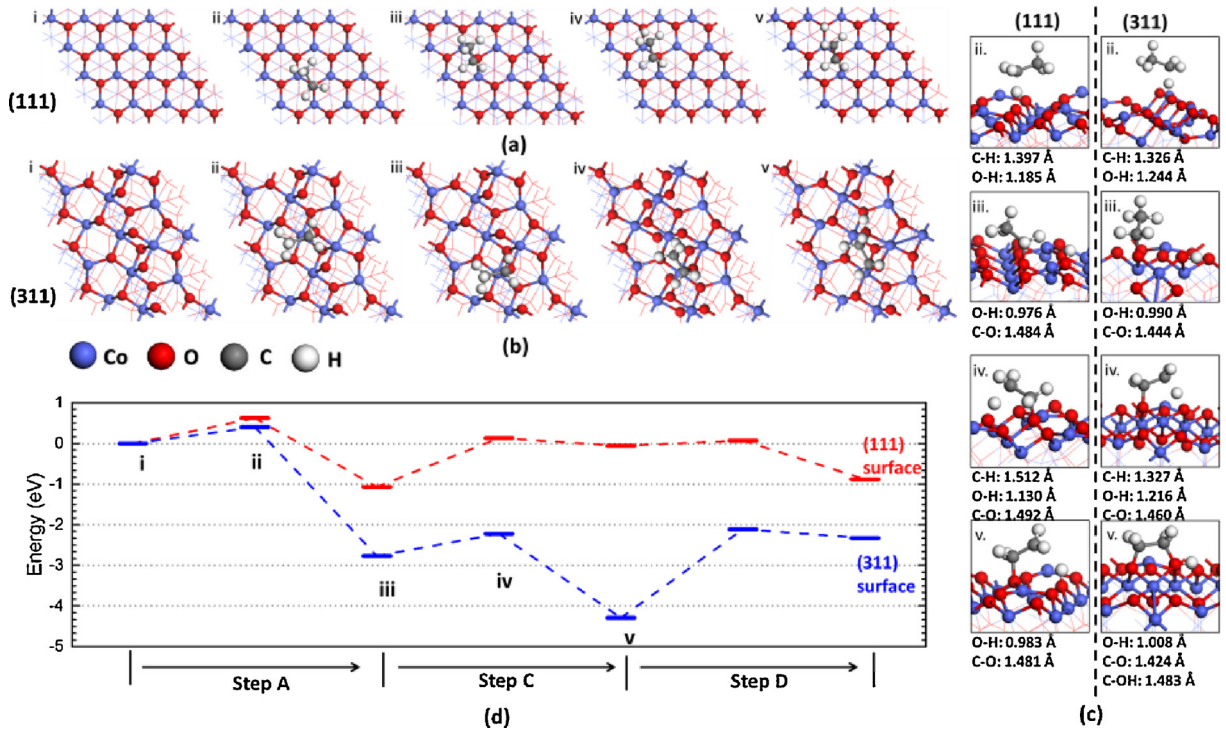

Fig. 11. Structures of transition states and final states of each step of reaction routines of A-C-D on (111) and (311) and their energy profiles. (a) Top view of structure i (bare surface), ii (transition state of step A, iii (final state of step A), iv (transition state of step C) and v (final state of step C) on (111) of Co_3O_4. (b) Top view of structure i (bare surface), ii (transition state of step A, iii (final state of step A), iv (transition state of step C) and v (final state of step C) on (311) of Co_3O_4. (c) Side views of structure i (bare surface), ii (transition state of step A, iii (final state of step A), iv (transition state of step C) and v (final state of step C) on (111) (left column) and (311) (right column) of Co_3O_4. (d) Energy profiles of A-C-D on (111) (red dashed line) and A-C-D on (311) (blue dashed line) (For interpretation of the references to colour in this figure legend, the reader is referred to the web version of this article).

Table 3
Activation energies (E_a) and reaction energies (ΔH) for the four key elementary steps in Fig.11.

Surface		Step A	Step B	Step C	Step D
111	E_a (eV)	0.62	0.87	1.20	0.13
	ΔH (eV)	—1.07	—0.37	1.01	—0.82
311	E_a (eV)	0.40	0.30	0.55	2.18
	ΔH (eV)	—2.77	—1.77	—1.52	1.96

scale, we can rationalize why (111) surface couldn't form a "deprotonated ethylene glycol"-like stable species although it does on (311). On the (311), the H—O*– is still active for binding with carbon atoms of —O*—CH_2—CH_2—O (Fig. S7). This is due to the fact that the number of Co atoms around an O atom is only 2 for c site of (311) (entry 3 of Table 2) instead of 3 of (111) (entry 1 of Table 2). Thus, the under-coordinated oxygen atoms can bond with carbon atom of —CH_2—CH_2—. Obviously, the presence of the under-coordinated lattice oxygen atoms is crucial in determining the selectivity for ODH, which is typically lack on facets formed at elevated temperatures.

The potential to form a "deprotonated ethylene glycol"-like stable intermediate is strongly related to the orientation of OH groups formed on (111) and (311). As the shown orientation of the H—O— group in Fig. S7a and v of (111) in Fig. 11c, the short distance between HO and the formed intermediate is not favorable for the formation of a "deprotonated ethylene glycol"-like stable species on (111). In addition, the pointing-away orientation of H—O— in v of (311) in Fig. 11c and Fig. S7c does not block the binding of the terminal C* of C*H_2—CH_2—O— to surface oxygen atom to form another C—O bond, by which a "deprotonated ethylene glycol"-like species is formed on (311).

As shown in Fig. S7b our calculations suggest that this is not impossible to form a "deprotonated ethylene glycol"-like species on (111); but the binding energy of —CH_2CH_2—, a part of the deprotonated ethylene glycol on (111) is much lower than that on (311) by 1.94 eV. The high binding energy of —CH_2—CH_2— on Co_3O_4 (311) results in a much high desorption barrier as shown in Fig. 11d, in contrast to the nearly barrier-less desorption of CH_2—CH_2— species from Co_3O_4(111). This is mainly due to the strong binding of ethylene on an under-coordinated oxygen atom with CN(O—Co) = 2 on (311) (Fig. S7c and S7d). These under-coordinated oxygen atoms exist on (311) but not on (111).

In the formed intermediate on (111) (Fig. S7a), only one carbon of the —O*—CH_2—CH_2 moiety remains sp^3, while the other carbon atom is now already in sp^2 hybridization and has a spin moment of 0.43 μ_B, suggesting the formation of an unpaired 2p electron on that carbon. In other words, "half of the ethylene molecule" is now formed on the (111) surface. The C—C bond distances shown in Fig. S8a and S8b also suggest the difference between bonding of the C_2H_4 moiety on (311) and (111). Obviously, the C—C bond of the intermediate formed on (111) approaches a double bond. Thus, our studies uncovered the fundamental difference in catalytic selectivity results from the difference in the local coordination environment of the active sites between (311) and (111). Tailoring surface structure through temperature-dependent faceting can thereby promote catalytic selectivity.

3.5. Durability and reusability of Co_3O_4-800 °C catalyst

Durability of catalytic performance and recyclability are two major concerns for a catalyst in practical applications. The activity and selectivity of ethane to ethylene on Co_3O_4-800 °C catalyst with time-on-stream test and reaction cycle test were performed to assess the durability and reusability of Co_3O_4-800 °C catalyst. As shown in Fig. 12a, catalytic conversion and selectivity of Co_3O_4-800 °C maintains ~63% in selectivity for production of ethylene and ~37% in conversion of

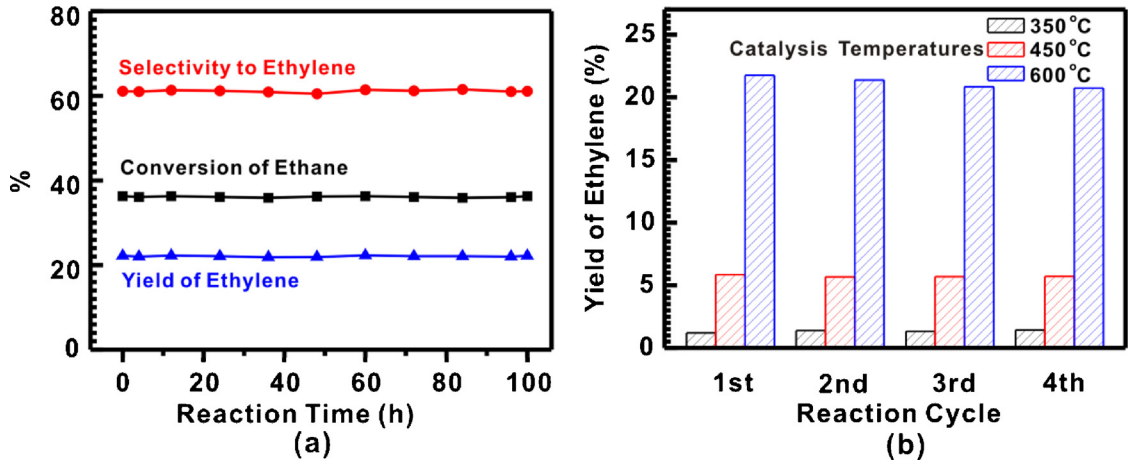

Fig. 12. Catalytic performances of Co_3O_4-800 °C catalyst in durability and reusability tests. (a) Conversion, selectivity and yield at catalysis temperature of 600 °C as a function of time in the first 100 *h*; (b) Plot of yields of ethylene in the first four cycles of test (The catalyst weight is 0.05 g diluted with 0.50 g quartz sand; the flow rate of C_2H_6 (10%) is 25.0 mL min^{-1} and the flow rate of O_2 (10%) is 25.0 mL min^{-1}).

ethane in the entire time span of the first 100 h, indicating a high durability. In addition, the reusability of the catalyst Co_3O_4-800 °C was tested in four reaction cycles. Catalytic conversion and selectivity were measured at 350, 450, and 600 °C in each of the four cycles in Fig. 12 b. There is no obvious change in catalytic performances in the four cycles, suggesting that Co_3O_4-800 °C catalyst has a quite high reusability in oxidative dehydrogenation of ethane to produce ethylene.

4. Summary

Through the integration of experimental macroscopic and microscopic studies of Co_3O_4 nanocrystals and DFT simulation of reaction pathways, temperature-dependent faceting of transition metal oxide was demonstrated to be an approach to tuning catalytic selectivity in partial oxidation for production of ideal products. In-situ studies of surface of Co_3O_4 nanocrystals using environmental TEM and ambient pressure XPS and isotope-labelled exchange of surface lattice oxygen revealed a temperature-dependent faceting. The rough, uneven, high Miller index surface (311) of Co_3O_4 nanocrystals was restructured to lower Miller surface (111) at 800 °C. The formed (111) exhibits active lattice oxygen atoms with significantly different chemical environments in contrast to (311). The distinctly different chemical and coordinating environment of oxygen atoms of (111) offer catalytic selectivity for generation of ethylene much higher than (311) by 30%–35%. DFT calculations suggest that the high catalytic selectivity results from the lower activation barrier in the rate-determining step in contrast to (311). The strong binding of $-CH_2-CH_2-$ on under-coordinated surface lattice atoms, O^C ($CN_{O-Co} = 2$) of (311) makes $-CH_2-CH_2$ be readily oxidized to CO or CO_2 due to a long residence time on (311). Thus, the selectivity for production of ethylene on (311) is lower than (111). This finding demonstrates a promising method to tune catalytic selectivity through controlling the coordination environment of surface lattice oxygen atoms since surface lattice oxygen atoms are active sites for oxidation reaction. For selective oxidation, the activity of surface lattice oxygen is crucial; overly active surface lattice oxygen would chemisorb ideal product molecules of selective oxidation such as ethylene, leading to further oxidation of ideal product molecules to final product CO_2 and H_2O instead of partial oxidation. The appropriate activity of surface lattice oxygen atoms is the key for achieving high selectivity for ideal product of partial oxidation reaction.

Acknowledgments

This work was mainly supported by the Chemical Sciences, Geosciences and Biosciences Division, Office of Basic Energy Sciences, Office of Science, U.S. Department of Energy, under Grant No. DE-SC0014561 and done at University of Kansas. This research used resources of the National Energy Research Scientific Computing Center, a DOE Office of Science User Facility supported by the Office of Science of the U.S. Department of Energy. *J*.L. and *J*.F. acknowledge the financial support from the National Natural Science Foundation of China (21703050 and 91545113).

Appendix A. Supplementary data

Supplementary material related to this article can be found, in the online version, at doi:https://doi.org/10.1016/j.apcatb.2018.05.013.

References

[1] G. Ertl, K. Knozinger, Handbook of Heterogeneous Catalysis, Wiley-VCH, 2008.
[2] F. Tao, S. Dag, L.-W. Wang, Z. Liu, D.R. Butcher, H. Bluhm, M. Salmeron, G.A. Somorjai, Science 327 (2010) 850–853.
[3] A.T. Bell, Science 299 (2003) 1688–1691.
[4] N. Mizuno, M. Misono, Chem. Rev. 98 (1998) 199–218.
[5] T. Schalow, M. Laurin, B. Brandt, S. Schauermann, S. Guimond, H. Kuhlenbeck, D.E. Starr, S.K. Shaikhutdinov, J. Libuda, H.J. Freund, Angew. Chem. Int. Ed. 44 (2005) 7601–7605.
[6] M. Behrens, F. Studt, I. Kasatkin, S. Kühl, M. Hävecker, F. Abild-Pedersen, S. Zander, F. Girgsdies, P. Kurr, B.-L. Kniep, Science 336 (2012) 893–897.
[7] T. Fujita, P. Guan, K. McKenna, X. Lang, A. Hirata, L. Zhang, T. Tokunaga, S. Arai, Y. Yamamoto, N. Tanaka, Nat. Mater. 11 (2012) 775–780.
[8] B.L. Hendriksen, M.D. Ackermann, R. van Rijn, D. Stoltz, I. Popa, O. Balmes, A. Resta, D. Wermeille, R. Felici, S. Ferrer, Nat. Chem. 2 (2010) 730–734.
[9] T. Rajh, L. Chen, K. Lukas, T. Liu, M. Thurnauer, D. Tiede, J. Phys. Chem. B 106 (2002) 10543–10552.
[10] F.F. Tao, M. Salmeron, Science 331 (2011) 171–174.
[11] J.A. Farmer, C.T. Campbell, Science 329 (2010) 933–936.
[12] Z.-P. Liu, P. Hu, J. Am. Chem. Soc. 125 (2003) 1958–1967.
[13] G.Aa.L. Somorjai, Introduction to Surface Chemistry and Catalysis, Wiley-VCH, 2010.
[14] F. Esch, S. Fabris, L. Zhou, T. Montini, C. Africh, P. Fornasiero, G. Comelli, R. Rosei, Science 309 (2005) 752–755.
[15] H.-J. Freund, G. Pacchioni, Chem. Sci. Rev. 37 (2008) 2224–2242.
[16] Q. Fu, H. Saltsburg, M. Flytzani-Stephanopoulos, Science 301 (2003) 935–938.
[17] M. Nolan, S.C. Parker, G.W. Watson, Surf. Sci. 595 (2005) 223–232.
[18] J.K. Nørskov, T. Bligaard, B. Hvolbæk, F. Abild-Pedersen, I. Chorkendorff, C.H. Christensen, Chem. Sci. Rev. 37 (2008) 2163–2171.
[19] G. Pacchioni, ChemPhysChem 4 (2003) 1041–1047.
[20] X. Pan, M.-Q. Yang, X. Fu, N. Zhang, Y.-J. Xu, Nanoscale 5 (2013) 3601–3614.
[21] S. Polarz, J. Strunk, V. Ischenko, M.W. Van den Berg, O. Hinrichsen, M. Muhler, M. Driess, Angew. Chem. Int. Ed. 45 (2006) 2965–2969.
[22] T. Punniyamurthy, S. Velusamy, J. Iqbal, Chem. Rev. 105 (2005) 2329–2364.
[23] S. Royer, D. Duprez, ChemCatChem 3 (2011) 24–65.
[24] V.V. Sysoev, B.K. Button, K. Wepsiec, S. Dmitriev, A. Kolmakov, Nano Lett. 6 (2006) 1584–1588.
[25] D. Wang, Z. Ma, S. Dai, J. Liu, Z. Nie, M.H. Engelhard, Q. Huo, C. Wang, R. Kou, J. Phys. Chem. C 112 (2008) 13499–13509.
[26] B. Yoon, H. Häkkinen, U. Landman, A.S. Wörz, J.-M. Antonietti, S. Abbet, K. Judai,

U. Heiz, Science 307 (2005) 403–407.
[27] M.V. Ganduglia-Pirovano, A. Hofmann, J. Sauer, Surf. Sci. Rep. 62 (2007) 219–270.
[28] M.T. Greiner, L. Chai, M.G. Helander, W.M. Tang, Z.H. Lu, Adv. Funct. Mater. 22 (2012) 4557–4568.
[29] S. Lee, C. Fan, T. Wu, S.L. Anderson, J. Am. Chem. Soc. 126 (2004) 5682–5683.
[30] A.L. Linsebigler, G. Lu, J.T. Yates, Chem. Rev. 95 (1995) 735–758.
[31] L. Liotta, M. Ousmane, G. Di Carlo, G. Pantaleo, G. Deganello, G. Marcì, L. Retailleau, A. Giroir-Fendler, Appl. Catal. A: Gen. 347 (2008) 81–88.
[32] N. Lopez, J.K. Nørskov, J. Am. Chem. Soc. 124 (2002) 11262–11263.
[33] B. Qiao, A. Wang, X. Yang, L.F. Allard, Z. Jiang, Y. Cui, J. Liu, J. Li, T. Zhang, Nat. Chem. 3 (2011) 634–641.
[34] T. Sayle, S. Parker, C. Catlow, Surf. Sci. 316 (1994) 329–336.
[35] R. Schaub, E. Wahlström, A. Rønnau, E. Lægsgaard, I. Stensgaard, F. Besenbacher, Science 299 (2003) 377–379.
[36] S.R. Zhang, J.J. Shan, Y. Zhu, L. Nguyen, W.X. Huang, H. Yoshida, S. Takeda, F. Tao, Nano Lett. 13 (2013) 3310–3314.
[37] F. Tao, P.A. Crozier, Chem. Rev. 116 (2016) 3487–3539.
[38] S.R. Zhang, L. Nguyen, Y. Zhu, S.H. Zhan, C.K. Tsung, F. Tao, Acc. Chem. Res. 46 (2013) 1731–1739.
[39] S.W. Cao, F. Tao, Y. Tang, Y.T. Li, J.G. Yu, Chem. Sci. Rev. 45 (2016) 4747–4765.
[40] F. Tao, S.R. Zhang, L. Nguyen, X.Q. Zhang, Chem. Sci. Rev. 41 (2012) 7980–7993.
[41] V. Fung, F.F. Tao, D. Jiang, Catal. Sci. Technol. 6 (2016) 6861–6869.
[42] D.E. Jiang, S. Dai, Phys. Chem. Chem. Phys. 13 (2011) 978–984.
[43] G. Kresse, J. Furthmuller, Phys. Rev. B 54 (1996) 11169–11186.
[44] G. Kresse, J. Furthmuller, Comp. Mater. Sci. 6 (1996) 15–50.
[45] J.P. Perdew, K. Burke, M. Ernzerhof, Phys. Rev. Lett. 77 (1996) 3865.
[46] G. Kresse, D. Joubert, Phys. Rev. B 59 (1999) 1758.
[47] P.E. Blöchl, Phys. Rev. B 50 (1994) 17953–17979.
[48] S.L. Dudarev, G.A. Botton, S.Y. Savrasov, C.J. Humphreys, A.P. Sutton, Phys. Rev. B 57 (1998) 1505.
[49] H.J. Monkhorst, J.D. Pack, Phys. Rev. B 13 (1976) 5188.
[50] G. Henkelman, H. Jónsson, J. Chem. Phys. 111 (1999) 7010.
[51] L. Hu, Q. Peng, Y. Li, J. Am. Chem. Soc. 130 (2008) 16136–16137.
[52] T. Li, S. Yang, L. Huang, B. Gu, Y. Du, Nanotechnology 15 (2004) 1479.
[53] W.-Y. Li, L.-N. Xu, J. Chen, Adv. Funct. Mater. 15 (2005) 851–857.
[54] N. Dahal, I.A. Ibarra, S.M. Humphrey, J. Mater. Chem. 22 (2012) 12675–12681.
[55] N. Du, H. Zhang, B. Chen, J. Wu, X. Ma, Z. Liu, Y. Zhang, D. Yang, X. Huang, J. Tu, Adv. Mater. 19 (2007) 4505–4509.
[56] T.A. Garibyan, L.Y. Margolis, Catal. Rev. Sci. Eng. 31 (1989) 355–384.
[57] M.D. Chen, W.Z. Li, J.F. Zhang, Y. Wu, X.D. Cao, H.L. Wan, Acta Chim. Sinica 62 (2004) 1760.
[58] K. Reuter, M. Scheffler, Phys. Rev. B 65 (2001) 035406.